BMC Oral Health

RESEARCH

Open Access

In vivo biocompatibility of elderberry-enriched carboxymethyl chitosan in soft tissue and calvaria bone defects

Bilge Cansu Uzun Saylan[1*], Gizem Baysan[2], Osman Yılmaz[3], Candan Efeoglu[4], Serap Cilaker Micili[5], Nevin Ersoy[6], Mustafa Mahmut Baris[7], Kaan Orhan[8] and Hasan Havitcioglu[2,9]

Abstract

Background Regeneration of soft and hard tissues remains a major challenge in periodontal and craniofacial applications, necessitating the development of multifunctional and biocompatible scaffolds. This study investigates the in vivo biocompatibility and regenerative potential of elderberry-enriched, polyethylene glycol diglycidyl ether (PEGDE)-crosslinked carboxymethyl chitosan (CMCht-E) in a rat model.

Methods Twenty-six eight-week-old female Wistar rats were randomly assigned to three experimental groups (subcutaneous, intramuscular, and calvarial; $n=7$ per group). In each rat, symmetrical 5 mm defects were created, with the biomaterial implanted on one side and the contralateral side serving as the control. A sham group ($n=5$) was included to account for surgical and imaging-related effects. Tissue responses were evaluated using ultrasonography, computed tomography (CT), micro-computed tomography (micro-CT), histomorphometry, and immunohistochemistry (CD68/CD163).

Results Soft tissue healing, confirmed by both ultrasonography and histological analysis, revealed similar characteristics between the biomaterial and control sites, suggesting a regenerative response closely resembling native tissue architecture. In the calvarial group, histomorphometric assessment and micro-CT analysis demonstrated a statistically significant increase in new bone formation in the CMCht-E group compared to controls ($p<0.05$). There were no significant differences in CD68 and CD163 expression between biomaterial and control groups ($p>0.05$).

Conclusion This first in vivo study demonstrates that CMCht-E is biocompatible and supports bone and soft tissue regeneration through controlled biodegradation. These findings highlight its promise as a naturally derived biomaterial for future use in periodontal and tissue engineering applications.

Keywords Elderberry, Carboxymethyl chitosan, Biocompatibility, Biomaterial, Bone regeneration, Soft tissue, Ultrasonography, Microcomputed tomography

*Correspondence:
Bilge Cansu Uzun Saylan
bilgecansu.uzunsaylan@deu.edu.tr

Full list of author information is available at the end of the article

© The Author(s) 2025. **Open Access** This article is licensed under a Creative Commons Attribution-NonCommercial-NoDerivatives 4.0 International License, which permits any non-commercial use, sharing, distribution and reproduction in any medium or format, as long as you give appropriate credit to the original author(s) and the source, provide a link to the Creative Commons licence, and indicate if you modified the licensed material. You do not have permission under this licence to share adapted material derived from this article or parts of it. The images or other third party material in this article are included in the article's Creative Commons licence, unless indicated otherwise in a credit line to the material. If material is not included in the article's Creative Commons licence and your intended use is not permitted by statutory regulation or exceeds the permitted use, you will need to obtain permission directly from the copyright holder. To view a copy of this licence, visit http://creativecommons.org/licenses/by-nc-nd/4.0/.

Background

Tissue engineering and regenerative medicine integrate biomaterials, stem cells, and bioactive agents to promote endogenous healing and offer biologically based alternatives to conventional therapies in dentistry and medicine [1–3]. Periodontitis, a chronic inflammatory disease with multifactorial etiology, leads to progressive destruction of the tooth-supporting structures, ultimately resulting in tooth loss if left untreated [4]. Effective regeneration of lost soft and hard tissues becomes essential in advanced periodontal defects. Periodontal regenerative techniques aim to restore periodontal tissues and function [5]. Autogenous bone grafts are considered the gold standard due to their osteoconductive, osteogenic, and osteoinductive properties; however, they pose clinical challenges such as donor site morbidity, limited availability, and surgical complexity [6]. As alternatives, allografts, xenografts, and synthetic materials are used, though they may elicit immune responses, fibrous encapsulation, or insufficient biomechanical performance [7, 8]. Guided tissue regeneration techniques were introduced to improve outcomes, combining bone grafts with barrier membranes to enhance selective tissue regrowth [9]. However, in cases of recurrent periodontal inflammation, inflammatory cell infiltration disrupts the histological integrity of healthy connective tissue and vascularization, negatively affecting the regenerative potential of the periodontal ligament and cementum [10, 11].

In periodontal tissue engineering, widely used scaffolding materials include natural biopolymers such as collagen, chitosan, and hyaluronic acid, along with synthetic alternatives like poly (lactic-co-glycolic acid) and polyethylene terephthalate [12, 13]. Chitin, the second most abundant biopolymer in nature after cellulose, is primarily derived from natural sources such as crustacean shells (e.g., shrimp, crab), insect exoskeletons, marine sponges, and fungal cell walls, including those of molds and yeasts [14]. Chitosan, obtained through the deacetylation of chitin, contains functional amino and hydroxyl groups that allow for a wide range of chemical modifications and contribute to its diverse biological activities [15, 16]. The degree of carboxymethylation enhances its water solubility without compromising the intrinsic properties of chitosan. Moreover, chitosan-based scaffolds can be easily formulated into structures such as hydrogels, gels, films, composites, and membranes, enabling broad applicability in tissue engineering [17, 18]. In the present study, the polymer matrix was based on carboxymethyl chitosan (CMCht) and crosslinked using polyethylene glycol diglycidyl ether (PEGDE). This water-soluble agent reacts with hydroxyl, amine, and carboxyl groups. PEGDE also facilitates surface functionalization by coupling hydroxyl groups with proteins. Although not a naturally derived crosslinker, PEGDE is widely used in the pharmaceutical and biomaterial industries due to its low toxicity profile [19].

The elderberry plant (*Sambucus nigra*) is well known for its potent antioxidant activity, as well as its richness in amino acids and vitamins [20, 21]. It is also a valuable source of B- and A-group vitamins, tocopherols, α-tocotrienol, vitamin C, and trace elements such as potassium, calcium, iron, magnesium, phosphorus, sodium, zinc, copper, manganese, selenium, chromium, nickel, and cadmium [22]. Elderberry has been reported to exhibit a wide range of biological properties, including antioxidant, anti-inflammatory, anti-allergic, immunomodulatory, antiviral, antibacterial, antidepressant, antidiabetic, anti-atherosclerotic, and hypoglycemic activities [23, 24]. In a study investigating the efficacy of elderberry extract against periodontal pathogens, the extract was shown to inhibit the release of pro-inflammatory cytokines [25] and suppress neutrophil activation, a key mechanism underlying periodontal tissue destruction [26].

A previous study comprehensively reported the in vitro characterization of the elderberry-enriched carboxymethyl chitosan (CMCht-E) polymer scaffold [27]. In that study, various formulations including CMCht, CMCht-H (hawthorn), and CMCht-E (elderberry) were systematically evaluated with respect to pore morphology, antioxidant capacity, enzymatic degradation, swelling behavior, and biological activity. Biocompatibility was confirmed by the sustained viability of mesenchymal stem cells over a 28-day in vitro period, with no evidence of cytotoxicity as determined by water-soluble tetrazolium salt-1 (WST-1), alkaline phosphatase (ALP), and glycosaminoglycan (GAG) assays. Among these formulations, CMCht-E exhibited the most promising profile, characterized by superior antioxidant capacity, enhanced extracellular matrix-related functionality, and demonstrated cytocompatibility. Building upon these findings, the present study was designed to evaluate the in vivo biocompatibility of CMCht-E in both soft tissue and calvarial bone environments, and to further explore its regenerative potential for future translational applications.

Methods

Preparation of the CMCht-E scaffold

A 2.5% (w/v) solution of CMCht (O-carboxymethylated chitosan, 90% deacetylation, Santa Cruz Biotechnology, cat. no. 358091) was completely dissolved in distilled water containing elderberry extract at a concentration of 0.05 mg/ml (w/v). The optimum concentration of the elderberry extract was determined based on our previous study [28]. The mixture was stirred with a magnetic stirrer for approximately 2 h until a homogeneous solution was achieved. The elderberry extract used in the CMCht-E formulation was powdered and derived from a 100%

ethanolic extraction (elderberry extract powder, 100 g; 100% natural; NatureHerb Store, China). The extract was commercially sourced.

Following solution preparation, 0.04 g of PEGDE (Sigma-Aldrich, 475696, Mn = 500) was added as a cross-linker to each 5 mL aliquot. The hydrogel structure was formed via cross-linking in a vacuum oven at 40 °C for 48 h. Subsequently, the samples were frozen at – 20 °C for approximately 12 h to ensure complete solidification. In the next step, lyophilization was performed at – 25 °C under 0.1 bar pressure for 48 h to obtain sponge-like scaffolds. This study provides comprehensive details on scaffold fabrication and material characterization, including chemical analysis [27]. Additional chemical characterization was performed using attenuated total reflectance Fourier transform infrared spectroscopy (ATR-FTIR), as presented in the supplementary data (Fig. 1). Once the hydrogel scaffolds were fully dried, they were cut into uniform dimensions (5 mm in diameter and 2 mm in thickness) using a biopsy punch for in vivo applications. Prior to implantation, the CMCht-E scaffolds were sterilized using ethylene oxide.

Animal experiments

The sample size was calculated using G*Power version 3.1.9 ($\alpha = 0.05$, power = 85%, effect size = 0.85), indicating that a minimum of 25 rats was required. To maintain equal group sizes and account for potential losses, 26 rats were included in the study.

All animals used in the study were laboratory-bred female Wistar rats (eight weeks old, 250–300 g), obtained from the Experimental Animal Laboratory of the Faculty of Medicine, Dokuz Eylul University (Izmir, Türkiye), where all procedures were conducted. The study protocol was approved by the Local Ethics Committee for Animal Experiments of Dokuz Eylul University (Approval No: 28-2023). A clinical trial number does not apply to this preclinical study. The ARRIVE 2.0 guidelines were followed for all animal procedures.

The rats were randomly assigned to three experimental groups—subcutaneous, intramuscular, and calvarial ($n = 7$ per group). A separate sham group ($n = 5$) was included to control for the effects of anesthesia, surgical intervention, and imaging procedures. In the sham group, only a subcutaneous skin incision was performed, and no biomaterial was implanted.

Animals were housed in standard cages under temperature-controlled conditions, with a 12-hour light/dark cycle and ad libitum access to food and water. Surgical procedures were performed under sterile conditions. Postoperatively, 5 mL of oral Paracetamol (OD) was added to the rats' drinking water for 15 days to provide analgesia. Surgical sites, as well as food and water intake, were monitored twice weekly throughout the experiment.

The body weights of all animals were recorded for 5 days postoperatively using a precision scale (CAS, ED-H model), and clinical signs were observed. Skin and muscle discoloration, edema, restricted mobility, piloerection, tenderness, discharge, and dehiscence were scored on a 0–5 scale (0 = no signs, 5 = severe). Animals that received a score of 5 at any time point or showed signs of compromised vital functions were excluded from the study.

Animals in the subcutaneous and intramuscular groups were sacrificed at week 4, while those in the calvarial group were sacrificed at week 8; body weights were also recorded at these time points. All rats within each experimental group were sacrificed simultaneously at the designated time point. Animals were euthanized using a high dose of anesthetic. Before euthanasia, 5 mL of blood was collected from the abdominal aorta into heparin-coated tubes for hematological analysis (WBC, RBC,

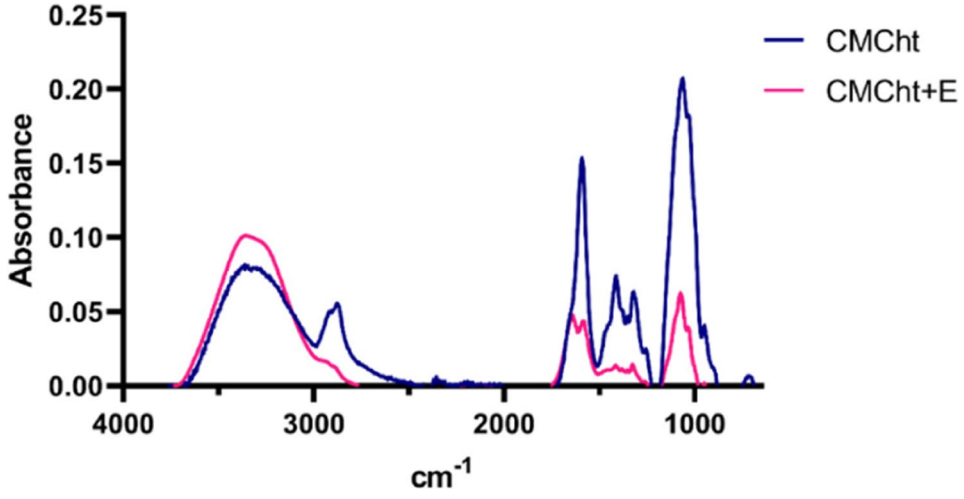


Fig. 1 Chemical characterization of the CMCht-E scaffold using attenuated total reflectance Fourier transform infrared spectroscopy (ATR-FTIR)

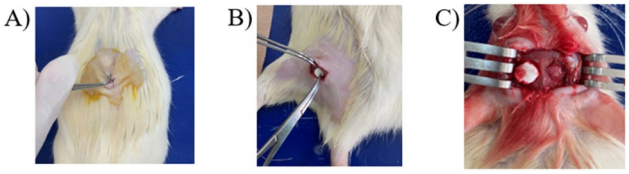


Fig. 2 Biomaterial implantation into the assigned experimental groups, Implantation sites: (**A**) subcutaneous, (**B**) intramuscular, (**C**) calvarium

HGB, MCV, MCH, MCHC, PLT, NE, LY, MO, EO). At necropsy, the skin and surrounding tissues of the surgical sites were examined for vascularization, erythema, edema, abscess, capsule formation, and scarring, using a binary scoring system (present/absent).

The surgical procedures were conducted by a periodontist (BCUS) and an oral and maxillofacial surgeon (CE). A veterinary physician (OY) carried out macroscopic wound healing assessment, necroscopic evaluation at the time of sacrifice, and blood collection for hemogram analysis. The physician was blinded to the group allocations to ensure an objective and unbiased assessment of the outcomes.

Anesthesia technique

Rats were anesthetized with a combination of ketamine (50 mg/kg) and xylazine (5 mg/kg) administered intraperitoneally. Sterile surgical technique was applied throughout the experiment. Rats were positioned prone on the operating table, and all surgical incisions were closed with 4 – 0 resorbable sutures (Pegelak®, 90% glycolide and 10% L-lactide, Turkey).

Subcutaneous implantation

In the dorsal interscapular region, a longitudinal skin incision of approximately 1 cm was created to access the subcutaneous tissue. A subcutaneous pocket was prepared, and a 5 mm diameter sterile tissue scaffold was implanted. The incision was closed with sutures (Fig. 2A). A second pocket, 3 cm caudally, was created as the control site. This pocket was left empty and sutured without material implantation.

Intramuscular implantation

Surgical access to the lateral surface of the left femur was achieved through a skin incision approximately 1 cm in length. The biceps femoris muscle was exposed, and its fascia and fibers were separated along the longitudinal axis to create a muscle pocket. A 5 mm diameter scaffold was inserted into this pocket. The scaffold adhered firmly without adhesives due to its hydrogel and hydrophilic nature. On the contralateral side (right femur), a similar defect was created and closed without material implantation (Fig. 2B).

Calvarium implantation

To expose the calvarium, a sagittal incision was made through the skin, galea, and periosteum. A 5 mm diameter critical-sized defect was prepared using a trephine bur (Meisinger, Germany) under saline irrigation on each side of the sagittal suture. The scaffold was placed in one defect, while the contralateral site remained empty as a control. The periosteum and skin were sutured (Fig. 2C).

Radiographic measurements

Radiographic evaluation included ultrasonography (USG), computed tomography (CT), and micro-computed tomography (micro-CT). USG and CT were performed under sevoflurane anesthesia to monitor early healing. Micro-CT was conducted post-mortem. Imaging evaluations (USG and CT) were conducted by a radiologist (MMB) from the Faculty of Medicine, blinded to group allocation. Micro-CT analyses were performed by a second oral and maxillofacial radiologist (KO) at a different institution (Ankara University), also blinded to the experimental groups.

Ultrasonography imaging

USG was performed on all rats at 9 days and 4 weeks post-implantation to assess tissue response and biocompatibility. High-resolution images were acquired at the subcutaneous (Fig. 3A), intramuscular (Fig. 3B), and calvarial (Fig. 3C) sites using the MS201 probe (up to 18 MHz). USG allowed for the evaluation of implant dimensions, peripheral vascularization, granulation tissue development, and potential encapsulation.



Fig. 3 USG imaging in rats: (**A**) subcutaneous, (**B**) intramuscular, (**C**) calvarium

Particular attention was given to identifying early signs of inflammation.

Computed tomography imaging

At 4 weeks, CT imaging was performed in the calvarial group using a Philips Brilliance SP 128 CT scanner under bone window settings. Defect area (mm^2) and circumference (mm) were measured in both the implanted and control sites to assess early bone healing.

Micro-computed tomography and analysis

Seven calvarial samples were scanned using a high-resolution desktop micro-computed tomography (micro-CT) system (Bruker Skyscan 1275, Kontich, Belgium). The scanning conditions were: 100 kVp, 100-mA, 0.5-mm Al/Cu filter, 9.1 µm pixel size, rotation at 0.2 step. Each sample was rotated 360˚ within an integration time of 5 min. The NRecon software (ver. 1.6.10.4, SkyScan, Kontich, Belgium) and CTAn (ver. 1.16.1.0, SkyScan) were used for the visualization and quantitative measurements of the samples. A total of 1,023 cross-sectional images were reconstructed from the entire volume using micro-CT. The CTAn (ver. 1.16.1.0, SkyScan) software was used for the visualization and analysis. All program specifications were used to analyze each sample's 2D and 3D microarchitecture. In the micro-CT analysis, regions of interest (ROIs) measuring 2 × 2 cm were manually selected based on consistent anatomical landmarks to encompass the calvarial defect area. Grayscale images were filtered using a Gaussian low-pass filter, and segmentation was performed through automatic thresholding (0–255 grayscale values), with the upper limit indicating the highest bone density. To ensure accurate 3D volume calculations, ROIs were interpolated and selected individually for each slice.

Measured structural parameters: percent bone volume (new bone formation) – BV/TV (%), bone surface-to-volume ratio – BS/BV (1/mm), bone surface density – BS/TV (1/mm), structure model index (SMI), trabecular thickness – Tb.Th (mm), trabecular number – Tb. N (1/mm), trabecular separation – Tb.Sp (mm), connectivity – Conn, and connectivity density – Conn.Dn ($1/mm^3$). Those parameters were calculated three-dimensionally (3D) based on the volume of the ROI. In addition, Bone Mineral Density (BMD) was calculated in the selected ROIs through the CTan program. The program automatically calculated mineral distributions using the shaping curve and HAP calibration phantoms (0.25 and 0.75 g/cm3). Then, the distributions of ROIs were compared.

Histological evaluation

Light microscopic examination method

Tissues were fixed in 10% buffered formaldehyde for 48–72 h. After routine histological procedures, the tissues were embedded in paraffin blocks. Sections with a thickness of 5 µm were obtained using a rotary microtome.[§] For histomorphological evaluation, sections were stained with hematoxylin [#] and eosin[¶] (H&E). Collagen deposition was evaluated using Masson's trichrome[‡] (MT) staining. Briefly, paraffin-embedded tissue sections were deparaffinized and rehydrated, stained according to the manufacturer's instructions, and examined under light microscopy. Collagen fibers appeared blue or green, muscle and cytoplasm red, and nuclei dark blue.

Histomorphological evaluation

This parameter's used to assess the amount of newly-formed blood to evaluate bone healing. Morphometric analysis of the newly formed tissue in the defect area was performed using the ImageJ software [29], and the assessments were independently conducted by two blinded histologists to ensure objectivity. At least five different regions were selected from each group, and images were captured using the same magnification for all sections. In each image, a standard-sized area, including the center of the defect border, was outlined. The surface area of the border was measured by selecting the ROI tool, and the measurement was recorded. Manual ROI selection was only used to delineate the defect area prior to thresholding, and care was taken to standardize this step by using anatomical landmarks. Within each selected area, the bone marrow cavities were identified and measured using the wand tracking tool, and this measurement was subtracted from the total area to determine the area covered solely by bone. Standardized protocols were followed for histomorphometric analysis using semi-automated measurements with ImageJ software, reducing subjective bias and improving measurement reproducibility. The resulting data were analyzed using the paired t-test in GraphPad Prism statistical software. A p-value of < 0.05 was considered statistically significant.

Immunohistochemical examination

The streptavidin-biotin-peroxidase assay used the primary antibodies against the CD68[*] and CD163[†]. After deparaffinization, sections were treated with trypsin[||] for 15 min, and endogenous peroxidase activity was blocked using a 0.3% solution of hydrogen peroxide in phosphate-buffered saline (PBS) at room temperature for 10 min. Then, the primary antibodies were applied for 2 h at 4 °C and subsequently washed with PBS. Afterward, the secondary antibody was applied for 30 min, followed by additional PBS washes. The peroxidase activity was visualized with diaminobenzidine.[§] Slides were counterstained with Mayer's hematoxylin, dehydrated, cleared, and analyzed on a light microscope. Two experienced observers who were blinded to the experimental groups independently performed both histological and immunohistochemical (IHC) evaluations. Prior to data collection,

the observers were calibrated using a subset of representative samples to ensure consistent evaluation criteria. In cases of disagreement, a consensus was reached through joint review.

Both the intensity and percentage of immunohistochemistry (IHC) staining were assessed. The staining intensity was scored as follows: 0 (no staining), 1 (weak staining), 2 (moderate staining), and 3 (intense staining). The percentage of stained cells was scored as follows: 0 (0% positive cells), 1 (1–10% positive cells), 2 (11–50% positive cells), 3 (51–80% positive cells), and 4 (81–100% positive cells). The final score was calculated by multiplying the percentage of positive cells by the intensity score [30].

§: RM 2255, Leica, CA, United States. #05–06002 L, Bio-Optica, Milano, Italy. ¶ 05–10,003 L, Bio-Optica, Milano, Italy.‡ Masson Trichrome Staining Set, 5022, GBL, Istanbul, Turkey. *BM4000S, Origene, Herford, Germany.†SM2106, Origene, Herford, Germany.||TA-125-TR, Thermo Fisher, Massachusetts, USA.‡‡‡‡85–9043, Invitrogen, Thermo Fisher, Massachusetts, USA. §§ 11,718,096,001, DAB Roche, Penzberg, Germany.

Statistical analysis

Data analysis was performed using the SPSS 27.0 statistical software package. Descriptive statistics for the evaluation results were expressed as mean and standard deviation. The normality of group distributions was assessed using the Kolmogorov-Smirnov test. For comparisons of numerical variables between two independent groups, the Student's t-test was employed when the assumption of normality was met; otherwise, the Mann-Whitney U test was used. For comparisons among three or more independent groups, one-way ANOVA was applied for normally distributed data, while the Kruskal-Wallis test was used when normality assumptions were not satisfied. In cases where significant differences were detected, post hoc Mann-Whitney analyses were conducted. Pearson correlation analysis was performed to evaluate the relationships between variables. A p-value of less than 0.05 was considered statistically significant.

Results

Postoperative results

No serious post-operative complications were observed. Feed and water consumption remained stable throughout the study period. In the calvarial defect group, mild post-operative symptoms—scored as 1 point—including subcutaneous ecchymosis, edema, and tenderness at the surgical site, were observed during the first three post-operative days. No abnormalities were detected in the control and biomaterial groups involving subcutaneous or intramuscular tissue (scored as 0 points).

Based on hemogram analysis, no statistically significant differences were observed between the sham and experimental groups ($p > 0.05$).

The mean body weights of each group, measured immediately before surgery, daily for five days post-operatively, and at the time of sacrifice, are presented in Table 1.

Radiographic results

Ultrasonography findings

On USG performed on day 9, no encapsulation, no signs of inflammation, or fluid accumulation were seen. There was no obvious heterogeneity in the subcutaneous tissue (Fig. 4A). Peripheral vascularization was observed in Fig. 4B. On day 9, the average dimensions of the biomaterial (Fig. 4E) across all experimental groups were measured as 9.62 ± 0.03 mm in the horizontal axis and 5.95 ± 0.12 mm in the vertical axis, with no significant differences observed between the groups ($p > 0.05$). A hypoechoic rim compatible with capsular granulation tissue was observed around the material, located intramuscularly (Fig. 4C). This area was hypervascular on Doppler, and the findings initially supported a granulomatous response.

The material placed in the defect at the calvarial level was observed, and it was observed that the material developed in a mushroom-like contour, giving an undulation extending towards the defect's surface. There were no obvious fluid or inflammation-supporting findings around it. Although no obvious granulation is observed, minimal granulator foci are present, but hypervascularity is not observed. Significant reflection was observed on

Table 1 Mean body weight changes during pre- and postoperative periods

Groups	Operation day (gr)	Post-op day 1 (gr)	Post-op day 2 (gr)	Post-op day 3 (gr)	Post-op day 4 (gr)	Post-op day 5 (gr)	Sacrification (gr)
Subcutaneous*(n = 7)*	277.4 ± 9.9	280.3 ± 10.8	289.9 ± 10.9	285.3 ± 11.6	284.7 ± 11,5	283.7 ± 13.9	305.2 ± 21.2
Intramuscular*(n = 7)*	279.3 ± 12.7	283.1 ± 11.2	290.4 ± 14.2	291.0 ± 17.3	286.0 ± 17,6	282.9 ± 16.0	305.0 ± 16.4
Calvarial *(n = 7)*	285.8 ± 22.9	271.1 ± 23.77	273.9 ± 19.4	278.4 ± 22.9	284.9 ± 23,9	281.3 ± 24.8	318.7 ± 27.8
Sham *(n = 5)*	286.3 ± 11.6	283.4 ± 13.9	286.6 ± 13.7	291.4 ± 11.9	296.8 ± 15,7	286.2 ± 13.2	306.6 ± 24.3

No statistical difference between and within the groups *(p > 0.05)*

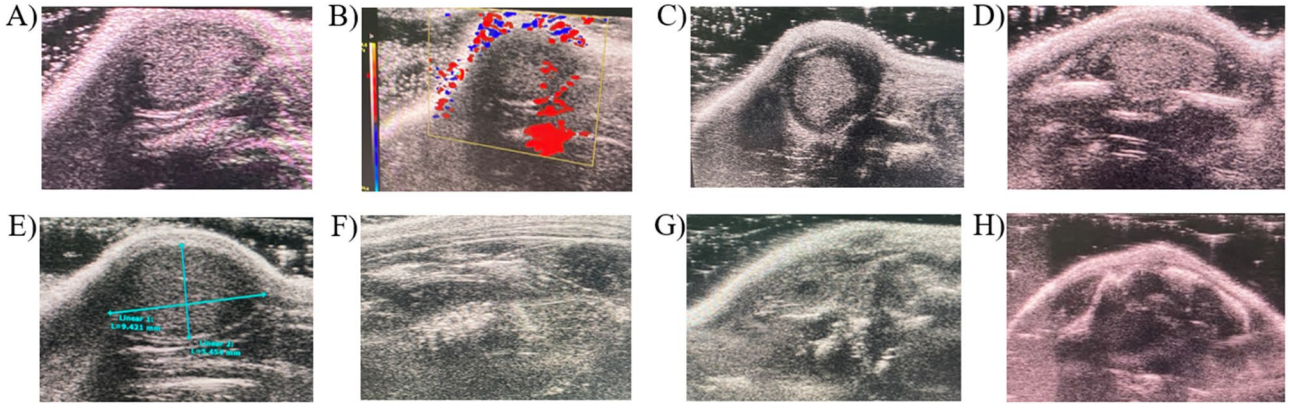


Fig. 4 Ultrasonographic findings in rats: **A** Subcutaneous biomaterial on day 9. **B** Vascularization around the subcutaneous biomaterial on day 9. **C** Intramuscular biomaterial on day 9. **D** Calvarial biomaterial on day 9. **E** Dimensions of the subcutaneous biomaterial at week 4. **F** Ultrasonographic view of subcutaneous tissue at week 4. **G** Ultrasonographic view of intramuscular tissue at week 4. **H** Ultrasonographic view of calvarial tissue at week 4

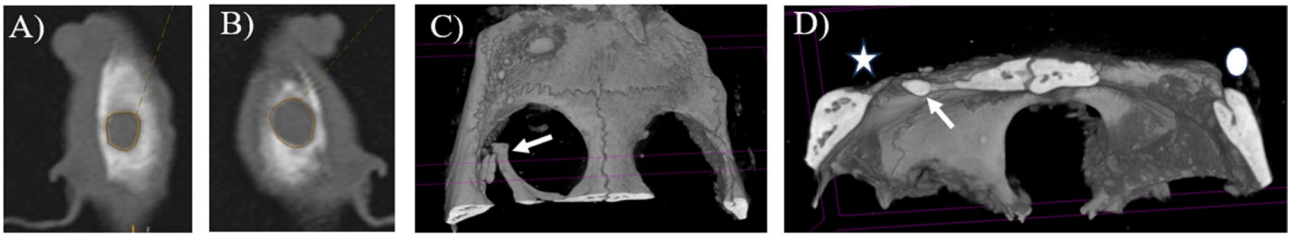


Fig. 5 (**A**) CT-based measurement of the calvarial defect in the biomaterial group at week 4. (**B**) CT-based measurement of the calvarial defect in the control group at week 4. (**C**) Micro-CT image of the calvarial bone at week 8; the white arrow indicates new bone formation in the biomaterial group. (**D**) Regarding the structure model index, the circular shape in the control defect indicates a more convex healing pattern. In contrast, the star-shaped section demonstrates that the biomaterial promotes a smoother healing line

the defect floor, and a newly formed internal tableau was observed with a dura or periosteal reaction in Fig. 4D.

USG was performed again 4 weeks after implantation in subcutaneous, intramuscular, and intrabony defects. The material was found to be completely resorbed, with no pathological formation in the surrounding subcutaneous (Fig. 4F), intramuscular (Fig. 4G), or calvarial tissues (Fig. 4H).

Computed tomography findings

CT scans performed at week 4 post-surgery revealed that the defect area in the biomaterial group (Fig. 5A) was significantly smaller (22.03 ± 0.44 mm^2) compared to the control group (Fig. 5B), which had an average defect area of 29.10 ± 0.87 mm^2 ($p < 0.05$).

Micro-computed tomography findings

Micro-CT images of the calvarial bone at week 8 are shown in Fig. 5C and D. Bone quality and density parameters for the biomaterial and control groups are compared in Table 2. Micro-CT analysis revealed a statistically significant difference in bone formation between the groups ($p < 0.05$).

Data obtained from micro-CT acquired parameters of bone formation show a statistically significant relationship. The percentage of new bone formation, trabecular thickness, trabecular linear density, connectivity, and connectivity density in the biomaterial group were significantly higher than those in the control group. In contrast, SMI was higher in the control group ($p < 0.05$) (Fig. 6).

Histological results

Evaluation of subcutaneous and intramuscular tissue implantation

Wound healing was similar in both the subcutaneous (Fig. 7) and intramuscular groups (Fig. 8), predominantly characterized by fibroblasts and mature collagen fibers (Figs. 7A–D and 8A–D). The presence of inflammatory cells, such as macrophages and lymphocytes, in the perivascular space was minimal. An increase in the number of blood vessels and connective tissue reactions was observed in both groups. No tumor-like tissue was detected. No notable difference was found in the immunohistochemical staining of CD163 and CD68 between the control and biomaterial groups ($p > 0.05$) (Figs. 7E–H and 8E–H).

Table 2 Statistical analysis of micro-CT acquired data

Analysis	Abbreviation	Unit	Biomaterial (*n* = 7)	Control (*n* = 7)	*p*-value
Percent bone volume (new bone formation)	BV/TV	%	5.63 ± 0.50	0.20 ± 0.07	0.001*
Bone mineral density	BMD	g/cm^3	2.16 ± 0.08	2.15 ± 0.08	0.855**
Bone surface/volume ratio	BS/BV	1/mm	9.84 ± 2.40	0.65 ± 0.12	<0.001**
Bone surface density	BS/TV	1/mm	0.63 ± 0.27	0.01 ± 0.03	0.001*
Structure model index	SMI	---	0.72 ± 0.43	2.00 ± 0.43	0.002*
Trabecular thickness	Tb.Th	mm	0.55 ± 0.09	0.19 ± 0.25	0.026*
Trabecular linear density	Tb.N	1/mm	0.32 ± 0.20	0.03 ± 0.04	0.001*
Trabecular separation	Tb.Sp	mm	1.91 ± 0.08	4.91 ± 0.52	<0.001**
Connectivity	Conn	---	331.57 ± 190.67	20.86 ± 8.96	0.005**
Connectivity density	Conn.Dn	1/mm^3	1.14 ± 0.65	0.25 ± 0.16	0.001*

* Mann Whitney U Test, ** Student's T Test $p < 0.05$ is statistically significant

Evaluation of bone tissue implantation

In the control group, well-vascularized connective tissue filled the bone defect, and osteoblast-like cells appeared occasionally (Fig. 9A). No inflammation or foreign body reaction was seen. In the biomaterial group, new bone formed around the defect and graft particles (Fig. 9B). MT staining showed similar bone healing and connective tissue development in both groups (Fig. 9C–D). No significant difference was observed in CD163 and CD68 immunohistochemical staining between the control and biomaterial groups ($p > 0.05$) (Fig. 9E–H). Analyses were conducted using the ImageJ program on MT-stained preparations to evaluate new bone formation. As shown in Fig. 10, new bone formation in the biomaterial group significantly increased compared to the healing rate observed in the control group ($p < 0.05$).

Scale bars: H&E and MT – 200 µm; CD163 and CD68 IHC – 50 µm.

Scale bars: H&E and MT – 200 µm; CD163 and CD68 IHC – 50 µm.

(C–D) MT staining of control and biomaterial groups; arrows indicate newly formed bone. (E–F) CD163 IHC staining; arrows indicate immunopositive cells. (G–H) CD68 IHC staining; arrows indicate immunopositive cells. RCT: reactive connective tissue.

Scale bars: H&E and MT – 200 µm; CD163 and CD68 IHC – 50 µm.

Discussion

In tissue engineering, biodegradable scaffolds that support cell attachment, proliferation, and differentiation promote tissue regeneration. These structures guide stem cell differentiation and support tissue repair by mimicking the extracellular matrix [12, 31]. Natural biomaterials are frequently preferred in periodontal tissue engineering due to their high biocompatibility, low cytotoxicity, and inherent biodegradability [32]. For successful alveolar ridge augmentation, biomaterials should be biocompatible, elicit minimal inflammation, and exhibit osteoconductive and osteoinductive properties. Solubility and

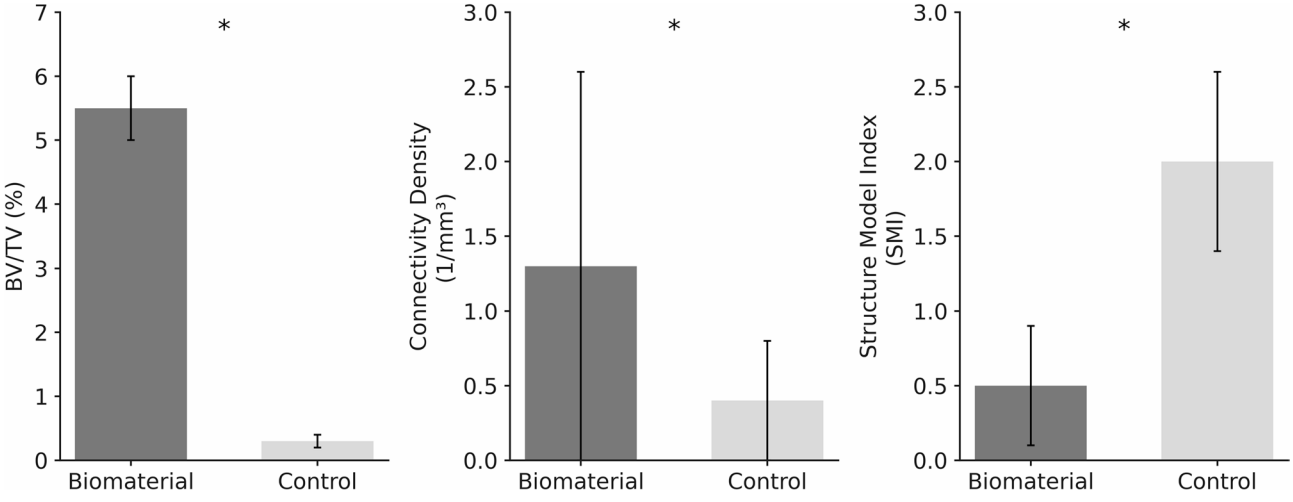


Fig. 6 Quantitative micro-CT analysis. BV/TV (%) and connectivity density were significantly increased in the biomaterial group, while the SMI was higher in the control group (*$p < 0.05$)

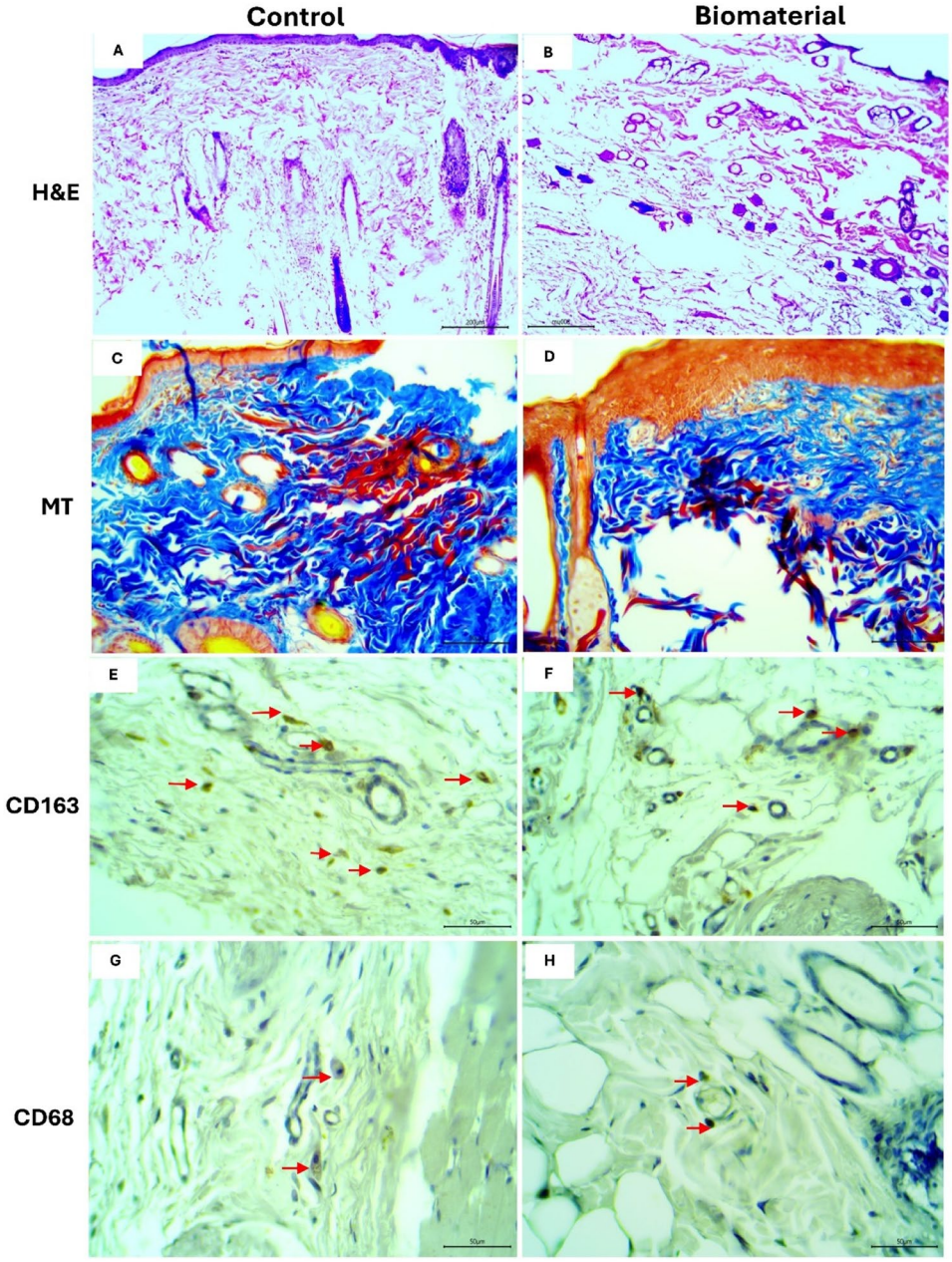


Fig. 7 Histological and IHC evaluation of subcutaneous tissue: (**A–B**) H&E staining of control and biomaterial groups. (**C–D**) MT staining of control and biomaterial groups. (**E–F**) CD163 IHC staining; arrows indicate immunopositive cells. (**G–H**) CD68 IHC staining; arrows indicate immunopositive cells

controlled biodegradability are critical parameters, as insufficient or delayed resorption may impair bone formation and increase inflammatory responses [33]. Natural polymers such as collagen, gelatin, alginate, and chitosan have found broad clinical application due to their bioactive structures that promote cellular interaction [34].

Chitosan is considered a promising material for tissue engineering applications as it has non-toxic, biocompatible, mucosal adhesive, and biodegradable properties that not only serve as a scaffolding material but also allow the initiation of new bone formation [35]. However, the poor water solubility of naturally derived chitosan in neutral pH conditions has been demonstrated as a disadvantage for clinical applications. Various chitosan derivative modification methods have been introduced to overcome this obstacle, such as sulfation, PEG-grafting, N- and O-hydroxylation, and O-carboxymethylation [36]. In the previous in vitro study, a PEDGE cross-linked form of elderberry-enriched CMCht was compared to plain CMCht scaffolds. The incorporation of elderberry extract increased the pore diameter from 196.62 μm to 309.10

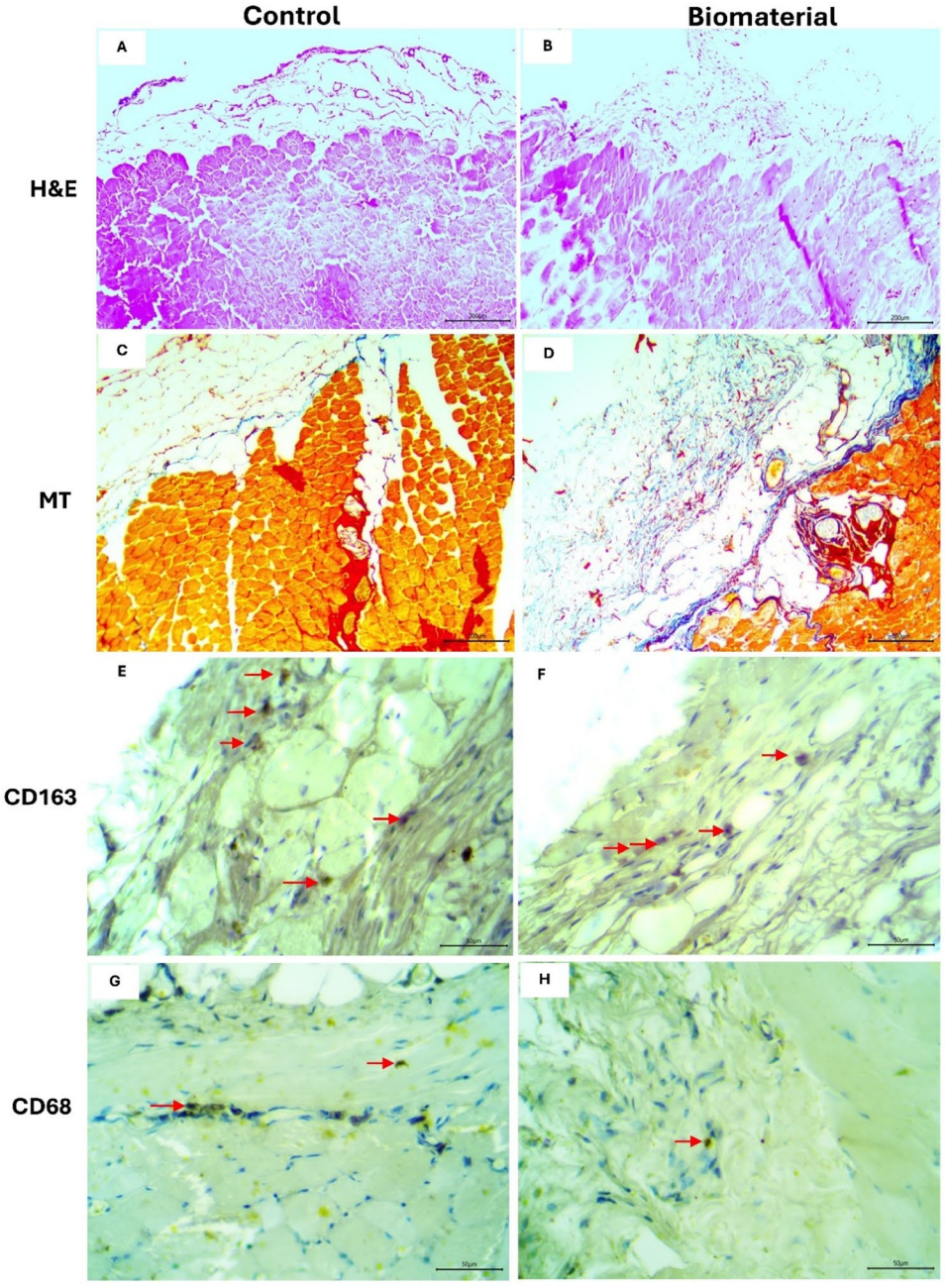


Fig. 8 Histological and IHC evaluation of intramuscular tissue: (**A–B**) H&E staining of control and biomaterial groups. (**C–D**) MT staining of control and biomaterial groups. (**E–F**) CD163 IHC staining; arrows indicate immunopositive cells. (**G–H**) CD68 IHC staining; arrows indicate immunopositive cells

μm and was associated with enhanced cell migration and proliferation, while also limiting the uncontrolled swelling of the biomaterial [27]. In the present study, USG measurements on day 9 demonstrated that the volume of the CMCht-E biomaterial (initial size: 5 mm × 2 mm) nearly doubled in all experimental groups. This finding can be attributed to the high hydrophilicity of the polysaccharide-based matrix [37]. By the fourth week, USG confirmed that the biomaterial had undergone resorption within both soft and hard tissues. These outcomes suggest that the scaffold's porous architecture facilitates cellular infiltration and progressive biodegradation, supporting the regenerative process.

Macrophages are among the first cell types to interact with biomaterials and play a central role in regulating tissue regeneration. They contribute to repair by modulating inflammation, supporting biomaterial integration with host tissue, and recruiting stem cells to promote new tissue formation. In addition, they regulate cytokine release and orchestrate the immune response [38,

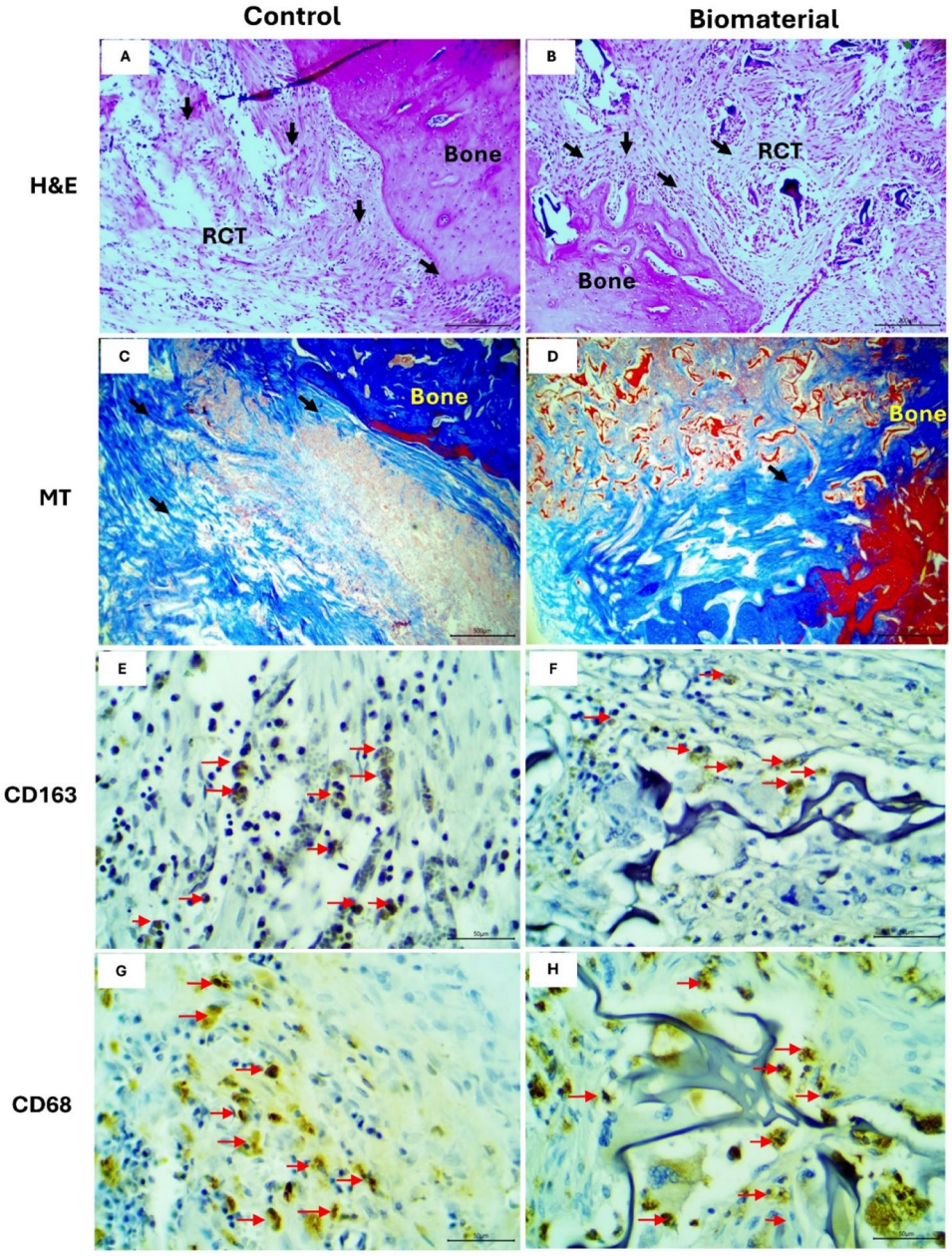


Fig. 9 Histological and IHC evaluation of calvarial bone defects: (**A–B**) H&E staining of control and biomaterial groups, respectively; arrows indicate newly formed bone

39]. M1 macrophages predominantly secrete pro-inflammatory factors and perform immune clearance functions to eliminate pathogens and tumor cells [40, 41]. In contrast, M2 macrophages release anti-inflammatory cytokines and growth factors, facilitating resolution of inflammation and promoting tissue healing, although excessive activation may lead to fibrosis and aberrant remodeling. CD163, mainly expressed on M2 macrophages, is involved in anti-inflammatory processes but has also been linked to carcinogenesis and tumor progression [42–44]. CD68 is a general macrophage marker identifying M1 and M2 subtypes [45, 46]. In our study, examination of CD68 and CD163 expression in biomaterials implanted into hard and soft tissues revealed no abnormal or pathological accumulation, with levels comparable to those observed in the control group. This indicates that the CMCht-E biomaterial did not elicit an exaggerated macrophage response when placed in subcutaneous, intramuscular, and calvarial defect areas. It did not induce a tumoral tissue reaction that could cause encapsulation around the biomaterial. Although this study did not analyze the specific phytochemicals in the

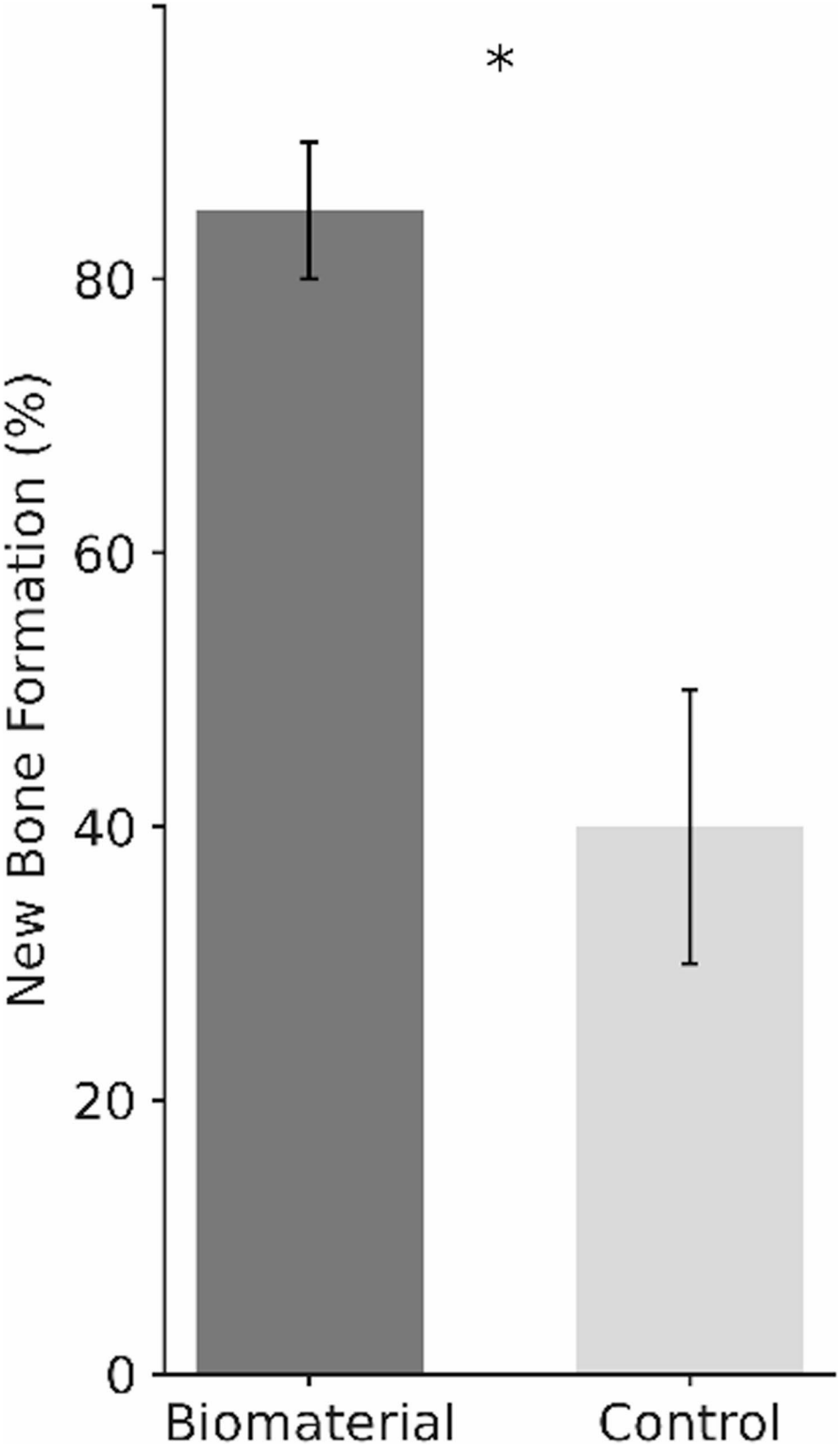


Fig. 10 Histomorphometric analysis of newly formed bone in calvarial defects. A statistically significant increase in newly formed bone was observed in the biomaterial group compared to the control group (*$p < 0.05$)

extract, the observed tissue compatibility may, in part, be attributed to the polyphenolic compounds of elderberry extract. These compounds have been shown to modulate inflammation and support tissue repair [47], possibly through balanced macrophage activity rather than by inducing excessive polarization [48]. However, further research is needed to determine whether the underlying mechanism involves direct macrophage polarization (e.g., M1 to M2 transition) in scaffold-guided tissue regeneration.

The successful incorporation of elderberry extract into the CMCht-E scaffold was confirmed by previous in vitro characterization data, indicating physical integration into the polymer matrix [27]. Furthermore, the scaffold exhibited a delayed degradation profile and sustained release behavior, suggesting that the extract was physically entrapped within the matrix, most likely due to interactions during lyophilization. Biologically, the superior antioxidant capacity of elderberry (4.74 μM AAE/mg), its demonstrated nontoxicity, and its positive effects on ALP activity and GAG in vitro, support its functional contribution to osteogenic potential. Another important finding from the in vitro analysis was also the increased expression of type I and II collagen observed via immunohistochemical staining, particularly in the elderberry-enriched scaffold (CMCht-E), highlighting the potent bioactivity of this formulation [27]. Taken together, these results, when evaluated in conjunction with the improved microstructural outcomes observed in vivo, strongly support both the physical integration and the regenerative relevance of elderberry within the scaffold design.

In the radiographic evaluation of chitosan biomaterial in rat calvaria by Chen et al., the amount of regenerated bone measured in the chitosan-treated group was significantly higher than that in the control group at the 3rd and 4th week. Regeneration of bone defects treated with chitosan from their surroundings and dural surface to cross-linked chitosan biomaterials has been demonstrated within 4 weeks [35]. Similarly, in our study, the CMCht-E biomaterial showed no signs of encapsulation on USG, and CT analysis at 4 weeks post-implantation in a cranial critical-size defect model revealed early bone regeneration [49], indicating effective healing promotion by the implanted scaffold. Ultrasonography was selected as a non-invasive, real-time imaging modality to monitor early soft tissue responses (e.g., inflammation, edema, vascularization) at the biomaterial implantation sites [50, 51]. While CT primarily provides information on mineralized tissue, USG offers superior resolution for soft tissue evaluation, particularly during the early healing phase. Therefore, it was also used to complement CT and micro-CT data in monitoring early inflammatory signs during the healing phase of hard tissue.

A desired characteristic of an ideal bone substitute is that it degrades at a controlled rate, allowing new bone tissue to grow, and that the degradation products are nontoxic [52]. Micro-CT analysis at the postoperative 8th week revealed a higher percentage of newly formed bone area (BV/TV) in the biomaterial-treated defects. Additionally, low values of SMI in the biomaterial-filled defects can signify that the ossification was more mature (plate-like trabecular structure) compared to the control group, which showed a higher SMI and a relatively more osteoporous structure (rod-like trabecular structure) [53]. CMCht-E biomaterial supported the direction of osteoblastic activity along the healing line in the defect area for smooth healing. The higher connectivity, connectivity density, and trabecular thickness in the biomaterial area indicate that the biomaterial physically supports the formation of new connections between surrounding structures, promotes regeneration, and serves as a physical bridge between trabecular components.

The healing effect of CMCht-E appears to stem from the complementary interaction between its structural composition and bioactive constituents. CMCht facilitates cell adhesion, biodegradation, and tissue integration critical for effective regeneration [54, 55]. The antioxidant and chemical profile of the elderberry extract was characterized in our previous study using FTIR spectroscopy and the 2,2-diphenyl-1-picrylhydrazyl (DPPH) assay, confirming the presence of phenolic and flavonoid compounds with bioactive potential [27]. These compounds exhibit potent antioxidant and anti-inflammatory properties, which are believed to create a favorable microenvironment for wound healing and osteogenesis by reducing oxidative stress and inflammation at the defect site [43]. In this context, histological analyses with H&E and MT staining revealed no evidence of foreign body reaction and confirmed new bone apposition around the scaffold. These attributes, including the ability of elderberry extract to modulate inflammation and regulate macrophage activity [56], may have contributed to the observed reduction in defect size and the enhancement of microstructural parameters, such as increased bone volume fraction (BV/TV) and trabecular connectivity, supporting the regenerative relevance of the CMCht-E scaffold.

Systemic safety is another critical aspect of biomaterial evaluation [57, 58]. In this study, body weights remained stable throughout the experimental period, and hematological parameters showed no significant differences between groups. Together with the absence of local adverse reactions, these findings suggest that the surgical procedures and the implanted CMCht-E scaffolds were well tolerated and did not elicit systemic adverse effects, thereby supporting the overall systemic biocompatibility of the material.

Although this study demonstrates the biocompatibility and regenerative potential of CMCht-E, some limitations should be acknowledged. The pro-angiogenic capacity was not tested in vitro with human umbilical vein endothelial cells (HUVEC) assays [1]; however, increased vascularization was observed by ultrasonography in vivo, consistent with previous reports on chitosan-based scaffolds [59]. Only female Wistar rats were used to minimize hormonal variability, which may limit generalizability [60–62], yet similar models have produced reproducible results in bone regeneration studies [63, 64]. A single PEGDE concentration was applied, based on the previously optimized and validated formulation reported by Gunes et al. [65], and mechanical performance was assessed only under dry conditions [27]; still, comparable studies report reliable outcomes for chitosan-based hydrogels in hydrated environments [66, 67]. Future investigations addressing these aspects will provide a more comprehensive understanding and strengthen CMCht-E's translational relevance for clinical use.

These findings provide compelling evidence of the CMCht-E scaffold's regenerative efficacy and translational relevance, particularly for maxillofacial, periodontal, and peri-implant applications.

Conclusion

This study highlights the potential of PEGDE-crosslinked, elderberry-enriched carboxymethyl chitosan as a multifunctional biomaterial for regenerative applications. Its design integrates biocompatibility, bioactivity, and controlled degradability, aligning with the fundamental principles of tissue engineering. These findings support further exploration of this scaffold system in translational research targeting dental and broader biomedical fields.

Abbreviations

PEGDE	Polyethylene glycol diglycidyl ether
CMCht	Carboxymethyl chitosan
CMCht-E	Elderberry-enriched carboxymethyl chitosan
ATR-FTIR	Attenuated total reflectance Fourier transform infrared spectroscopy
WST-1	Water-soluble tetrazolium salt-1
ALP	Alkaline phosphatase
DPPH	2,2-diphenyl-1-picrylhydrazyl
GAG	Glycosaminoglycan
USG	Ultrasonography
ROI	Region of interest
CT	Computed tomography
micro-CT	Micro-computed tomography
H&E	Hematoxylin and eosin
MT	Masson's trichrome
BMD	Bone mineral density
HUVECs	Human umbilical vein endothelial cells
WBC	White blood cell
RBC	Red blood cell
HGB	Hemoglobin
MCV	Mean corpuscular volume
MCH	Mean corpuscular hemoglobin
MCHC	Mean corpuscular hemoglobin concentration
PLT	Platelet count
NE	Neutrophils
LY	Lymphocytes
MO	Monocytes
EO	Eosinophils

Supplementary Information

The online version contains supplementary material available at https://doi.org/10.1186/s12903-025-06991-3.

Supplementary Material 1.

Acknowledgements

We thank Dr. Serdar Karakullukçu, M.D. for his assistance with statistical analysis and valuable comments.

Authors' contributions

BCUS: Writing – original draft; Investigation; Project administration; Funding acquisition; Methodology. OY: Data curation; Methodology; Resources; Investigation; Conceptualization. GB: Resources; Methodology. CE: Writing – review and editing; Investigation; Data curation. SCM, NE, KO, MMB: Data curation. HH: Conceptualization; Supervision.

Funding

The Research Fund of the Dokuz Eylul University supported this research (Project Number: 3274-Izmir, Turkey).

Data availability

All data generated or analyzed during this study are included in this published article.

Declarations

Ethics approval and consent to participate

The experimental protocol was approved by the Ethics Committee in Animal Use (28-2023) at the Experimental Animal Laboratory, Faculty of Medicine, Dokuz Eylul University, where all experimental procedures were carried out.

Consent for publication

Not applicable.

Competing interests

The authors declare no competing interests.

Author details

[1]Faculty of Dentistry, Department of Periodontology, Dokuz Eylül University, Izmir, Turkey
[2]Institute of Health Science, Department of Biomechanics, Dokuz Eylül University, Izmir, Turkey
[3]Faculty of Medicine Experimental Animals Laboratory, Dokuz Eylül University, Izmir, Turkey
[4]Faculty of Dentistry, Department of Oral and Maxillofacial Surgery, Dokuz Eylül University, Izmir, Turkey
[5]Faculty of Medicine, Department of Histology and Embryology, Dokuz Eylül University, Izmir, Turkey
[6]Faculty of Medicine, Department of Histology and Embryology, İzmir Tınaztepe University, Izmir, Turkey
[7]Faculty of Medicine, Department of Radiology, Dokuz Eylül University, Izmir, Turkey
[8]Faculty of Dentistry, Department of Oral and Maxillofacial Radiology, Ankara University, Izmir, Turkey
[9]Faculty of Medicine, Department of Orthopedics and Traumatology, Dokuz Eylül University, Izmir, Turkey

Received: 13 June 2025 / Accepted: 15 September 2025
Published online: 09 October 2025

References

1. Huang L, Gong W, Huang G, Li J, Wu J, Wang Y, et al. The additive effects of photobiomodulation and bioactive glasses on enhancing early angiogenesis. Biomed Mater. 2022. https://doi.org/10.1088/1748-605X/ac6b07.
2. Deng Y, Liang Y, Liu X. Biomaterials for periodontal regeneration. Dent Clin North Am. 2022. https://doi.org/10.1016/j.cden.2022.05.011.
3. Baysan G, Colpankan Gunes O, Akokay P, Husemoglu RB, Ertugruloglu P, Ziylan Albayrak A, et al. Loofah-chitosan and Poly (– 3-hydroxybutyrate-co-3-hydroxyvalerate) (PHBV) based hydrogel scaffolds for meniscus tissue engineering applications. Int J Biol Macromol. 2022. https://doi.org/10.1016/j.ijbiomac.2022.09.031.
4. Kwon T, Lamster IB, Levin L. Current concepts in the management of periodontitis. Int Dent J. 2021. https://doi.org/10.1111/idj.12630.
5. Kantarci A. Biological basis of periodontal regeneration. Dent Clin North Am. 2022. https://doi.org/10.1016/j.cden.2021.08.001.
6. Tournier P, Guicheux J, Paré A, Maltezeanu A, Blondy T, Veziers J, et al. A partially demineralized allogeneic bone graft: in vitro osteogenic potential and preclinical evaluation in two different intramembranous bone healing models. Sci Rep. 2021. https://doi.org/10.1038/s41598-021-84039-6.
7. Solyom E, Szalai E, Czumbel ML, Szabo B, Váncsa S, Mikulas K, et al. The use of autogenous tooth bone graft is an efficient method of alveolar ridge preservation – meta-analysis and systematic review. BMC Oral Health. 2023. https://doi.org/10.1186/s12903-023-02930-2.
8. Ciszyński M, Dominiak S, Dominiak M, Gedrange T, Hadzik J. Allogenic bone graft in dentistry: A review of current trends and developments. Int J Mol Sci. 2023. https://doi.org/10.3390/ijms242316598.
9. Ren Y, Fan L, Alkildani S, Liu L, Emmert S, Najman S, et al. Barrier membranes for guided bone regeneration (GBR): A focus on recent advances in collagen membranes. Int J Mol Sci. 2022. https://doi.org/10.3390/ijms232314987.
10. Van Dyke TE, Hasturk H, Kantarci A, Freire MO, Nguyen D, Dalli J, et al. Proresolving nanomedicines activate bone regeneration in periodontitis. J Dent Res. 2015. https://doi.org/10.1177/0022034514557331.
11. Jepsen K, Sculean A, Jepsen S. Complications and treatment errors related to regenerative periodontal surgery. Periodontol 2000. 2003. https://doi.org/10.1111/prd.12504.
12. Chen H, Song G, Xu T, Meng C, Zhang Y, Xin T, et al. Biomaterial scaffolds for periodontal tissue engineering. J Funct Biomater. 2024. https://doi.org/10.3390/jfb15080233.
13. Signorini L, Marenzi G, Facente A, Marrelli B, Marano RM, Valletta A, et al. Critical overview on pure Chitosan-based scaffolds for bone tissue engineering: clinical insights in dentistry. Int J Med Sci. 2023. https://doi.org/10.7150/ijms.87978.
14. Mu L, Wu L, Wu S, Ye Q, Zhong Z. Progress in chitin/chitosan and their derivatives for biomedical applications: where we stand. Carbohydr Polym. 2024. https://doi.org/10.1016/j.carbpol.2024.122233.
15. Atia GAN, Shalaby HK, Zehravi M, Ghobashy MM, Attia HAN, Ahmad Z et al. Drug-Loaded Chitosan Scaffolds for Periodontal Tissue Regeneration. Polymers (Basel). 2022. https://doi.org/10.3390/polym14153192
16. Zhu Y, Zhang Y, Zhou Y. Application progress of modified Chitosan and its composite biomaterials for bone tissue engineering. Int J Mol Sci. 2022. https://doi.org/10.3390/ijms23126574.
17. Geng Y, Xue H, Zhang Z, Panayi AC, Knoedler S, Zhou W, et al. Recent advances in carboxymethyl chitosan-based materials for biomedical applications. Carbohydr Polym. 2023. https://doi.org/10.1016/j.carbpol.2023.120555.
18. Sharma S, Kumar A, Deepak, Kumar R, Rana NK, Koch B. Development of a novel Chitosan based biocompatible and self-healing hydrogel for controlled release of hydrophilic drug. Int J Biol Macromol. 2018. https://doi.org/10.1016/j.ijbiomac.2018.05.020.
19. Kim D-H, Han J-H, Kwon H-C, Lim S-J, Han S-G, Jung H-S, et al. Toxicity assessment of a single dose of Poly(ethylene glycol) diglycidyl ether (PEGDE) administered subcutaneously in mice. Toxics. 2021. https://doi.org/10.3390/toxics9120354.
20. Marțiș Petruț GS, Mureșan V, Marc Vlaic RM, Mureșan CC, Pop CR, Buzgău G et al. The Physicochemical and Antioxidant Properties of Sambucus nigra L. and Sambucus nigra Haschberg during Growth Phases: From Buds to Ripening. Antioxidants (Basel). 2021. https://doi.org/10.3390/antiox10071093
21. Ferreira SS, Martins-Gomes C, Nunes FM, Silva AM. Elderberry (Sambucus Nigra L.) extracts promote anti-inflammatory and cellular antioxidant activity. Food Chem X. 2022. https://doi.org/10.1016/j.fochx.2022.100437.
22. Liu D, He X-Q, Wu D-T, Li H-B, Feng Y-B, Zou L, et al. Elderberry (Sambucus Nigra L.): bioactive Compounds, health Functions, and applications. J Agric Food Chem. 2022. https://doi.org/10.1021/acs.jafc.2c00010.
23. Stępień AE, Trojniak J, Tabarkiewicz J, Health-Promoting, Properties. Anti-Inflammatory and anticancer properties of Sambucus Nigra L. Flowers and fruits. Molecules. 2023. https://doi.org/10.3390/molecules28176235.
24. Wójciak M, Ziemlewska A, Zagórska-Dziok M, Nizioł-Łukaszewska Z, Szczepanek D, Oniszczuk T, et al. Anti-Inflammatory and protective effects of water extract and bioferment from Sambucus Nigra fruit in LPS-Induced human skin fibroblasts. Int J Mol Sci. 2023. https://doi.org/10.3390/ijms241210286.
25. Chaushu L, Weinreb M, Beitlitum I, Moses O, Nemcovsky CE. Evaluation of a topical herbal patch for soft tissue wound healing: an animal study. J Clin Periodontol. 2015. https://doi.org/10.1111/jcpe.12372.
26. Harokopakis E, Albzreh MH, Haase EM, Scannapieco FA, Hajishengallis G. Inhibition of Proinflammatory activities of major periodontal pathogens by aqueous extracts from elder flower (Sambucus nigra). J Periodontol. 2006. https://doi.org/10.1902/jop.2006.050232.
27. Baysan G, Yilmaz PA, Husemoglu RB, Albayrak AZ, Sisman AR, Havitcioglu H. Elderberry (Sambucus nigra) and Hawthorn (Crataegus oxyacantha) extract additives in carboxymethyl Chitosan scaffolds for osteochondral tissue engineering applications. J Appl Polym Sci. 2024. https://doi.org/10.1002/app.55637.
28. Baysan G, Husemoglu B, Havitcioglu H. Cytotoxic effects of Hawthorn and Elderberry extracts on 3T3 fibroblast cell line. J Med Innov Technol. 2020;2(1):85–91.
29. Starecki M, Schwartz JA, Grande DA. Evaluation of Amniotic-Derived membrane biomaterial as an adjunct for repair of critical sized bone defects. Adv Orthop Surg. 2014. https://doi.org/10.1155/2014/572586.
30. Hou T, Liang D, He J, Chen X, Zhang Y. Primary peritoneal serous carcinoma: a clinicopathological and immunohistochemical study of six cases. Int J Clin Exp Pathol. 2012;5(8):762-769.
31. Tavelli L, McGuire MK, Zucchelli G, Rasperini G, Feinberg SE, Wang H, et al. Extracellular matrix-based scaffolding technologies for periodontal and peri-implant soft tissue regeneration. J Periodontol. 2020. https://doi.org/10.1002/JPER.19-0351.
32. Abedi N, Rajabi N, Kharaziha M, Nejatidanesh F, Tayebi L. Layered scaffolds in periodontal regeneration. J Oral Biol Craniofac Res. 2022. https://doi.org/10.1016/j.jobcr.2022.09.001.
33. Suzuki O, Hamai R, Sakai S. The material design of octacalcium phosphate bone substitute: increased dissolution and osteogenecity. Acta Biomater. 2023. https://doi.org/10.1016/j.actbio.2022.12.046.
34. Zhang Y, Cheng X, Wang J, Wang Y, Shi B, Huang C, et al. Novel chitosan/collagen scaffold containing transforming growth factor-beta1 DNA for periodontal tissue engineering. Biochem Biophys Res Commun. 2006. https://doi.org/10.1016/j.bbrc.2006.03.106.
35. Chen C-K, Chang N-J, Wu Y-T, Fu E, Shen E-C, Feng C-W, et al. Bone formation using Cross-Linked Chitosan scaffolds in rat calvarial defects. Implant Dent. 2018. https://doi.org/10.1097/ID.0000000000000670.
36. de Abreu FR, Campana-Filho SP. Characteristics and properties of carboxymethylchitosan. Carbohydr Polym. 2009. https://doi.org/10.1016/j.carbpol.2008.06.009.
37. Neumann K. The case for poly(ylides) as a class of charge-neutral, hydrophilic polymers with applications in biomaterials science. Biomater Sci. 2024. https://doi.org/10.1039/d4bm00928b.
38. Abaricia JO, Shah AH, Chaubal M, Hotchkiss KM, Olivares-Navarrete R. Wnt signaling modulates macrophage polarization and is regulated by biomaterial surface properties. Biomaterials. 2020. https://doi.org/10.1016/j.biomaterials.2020.119920.
39. Davies LC, Jenkins SJ, Allen JE, Taylor PR. Tissue-resident macrophages. Nat Immunol. 2013. https://doi.org/10.1038/ni.2705.
40. Garaicoa-Pazmino C, Fretwurst T, Squarize CH, Berglundh T, Giannobile WV, Larsson L, et al. Characterization of macrophage polarization in periodontal disease. J Clin Periodontol. 2019. https://doi.org/10.1111/jcpe.13156.
41. Sheikh Z, Brooks PJ, Barzilay O, Fine N, Glogauer M. Macrophages, foreign body giant cells and their response to implantable biomaterials. Mater (Basel). 2015. https://doi.org/10.3390/ma8095269.
42. Liu J, Chen B, Bao J, Zhang Y, Lei L, Yan F. Macrophage polarization in periodontal ligament stem cells enhanced periodontal regeneration. Stem Cell Res Ther. 2019. https://doi.org/10.1186/s13287-019-1409-4.
43. Su C, Jia S, Liu H. Immunolocalization of CD163 + Tumor-Associated macrophages and symmetric proliferation of Ki-67 as biomarkers to differentiate new different grades of laryngeal dysplasia. Am J Clin Pathol. 2017. https://doi.org/10.1093/ajcp/aqx107.

44. Ham JS, Park HY, Ryu KJ, Ko YH, Kim WS, Kim SJ. Elevated serum interleukin-10 level and M2 macrophage infiltration are associated with poor survival in angioimmunoblastic T-cell lymphoma. Oncotarget. 2017. https://doi.org/10.18632/oncotarget.19301.
45. Galarraga-Vinueza ME, Obreja K, Ramanauskaite A, Magini R, Begic A, Sader R, et al. Macrophage polarization in peri-implantitis lesions. Clin Oral Investig. 2021. https://doi.org/10.1007/s00784-020-03556-2.
46. Fretwurst T, Garaicoa-Pazmino C, Nelson K, Giannobile WV, Squarize CH, Larsson L et al. Characterization of macrophages infiltrating peri-implantitis lesions. 2020. https://doi.org/10.1111/clr.13568
47. Osman AG, Avula B, Katragunta K, Ali Z, Chittiboyina AG, Khan IA. Elderberry extracts: characterization of the polyphenolic chemical Composition, quality Consistency, Safety, Adulteration, and Attenuation of oxidative Stress- and Inflammation-Induced health disorders. Molecules. 2023. https://doi.org/10.3390/molecules28073148.
48. Haş IM, Teleky B-E, Szabo K, Simon E, Ranga F, Diaconeasa ZM, et al. Bioactive potential of Elderberry (Sambucus Nigra L.): Antioxidant, antimicrobial Activity, bioaccessibility and prebiotic potential. Molecules. 2023. https://doi.org/10.3390/molecules28073099.
49. Fernández MP, Witte F, Tozzi G. Applications of X-ray computed tomography for the evaluation of biomaterial-mediated bone regeneration in critical-sized defects. J Microsc. 2020. https://doi.org/10.1111/jmi.12844.
50. Aparisi Gómez MP, Errani C, Lalam R, Vasilevska Nikodinovska V, Fanti S, Tagliafico AS, et al. The role of ultrasound in the diagnosis of soft tissue tumors. Semin Musculoskelet Radiol. 2020. https://doi.org/10.1055/s-0039-3402060.
51. Estrada H, Rebling J, Turner J, Razansky D. Broadband acoustic properties of a murine skull. Phys Med Biol. 2016. https://doi.org/10.1088/0031-9155/61/5/1932.
52. Zhang N, Zhao D, Liu N, Wu Y, Yang J, Wang Y, et al. Assessment of the degradation rates and effectiveness of different coated Mg-Zn-Ca alloy scaffolds for in vivo repair of critical-size bone defects. J Mater Sci Mater Med. 2018. https://doi.org/10.1007/s10856-018-6145-2.
53. Hildebrand T, Rüegsegger P. Quantification of bone microarchitecture with the structure model index. Comput Methods Biomech Biomed Engin. 1997. https://doi.org/10.1080/01495739708936692.
54. Kłosiński KK, Wach RA, Kruczkowska W, Duda Ł, Kołat D, Kałuzińska-Kołat Ż, et al. Carboxymethyl Chitosan hydrogels for effective wound Healing—An animal study. J Funct Biomater. 2023. https://doi.org/10.3390/jfb14090473.
55. Shariatinia Z. Carboxymethyl chitosan: properties and biomedical applications. Int J Biol Macromol. 2018. https://doi.org/10.1016/j.ijbiomac.2018.09.131.
56. Ho GTT, Wangensteen H, Barsett H, Elderberry, Extracts E. Phenolic Compounds, and metabolites and their effect on Complement, RAW 264. 7 macrophages and dendritic cells. 2017. https://doi.org/10.3390/ijms18030584
57. Sandker MJ, Duque LF, Redout EM, Chan A, Que I, Löwik CWGM, et al. Degradation, intra-articular retention and biocompatibility of monospheres composed of [PDLLA-PEG-PDLLA]-b-PLLA multi-block copolymers. Acta Biomater. 2017. https://doi.org/10.1016/j.actbio.2016.11.003.
58. Zieglowski L, Kümmecke AM, Ernst L, Palme R, Weiskirchen R, Talbot SR, et al. Assessing the severity of laparotomy and partial hepatectomy in male rats-A multimodal approach. PLoS ONE. 2021. https://doi.org/10.1371/journal.pone.0255175.
59. Aussel A, Thébaud NB, Bérard X, Brizzi V, Delmond S, Bareille R, et al. Chitosan-based hydrogels for developing a small-diameter vascular graft: *in vitro* and *in vivo* evaluation. Biomed Mater. 2017. https://doi.org/10.1088/1748-605X/aa78d0.
60. Townsend JM, Dennis SC, Whitlow J, Feng Y, Wang J, Andrews B, et al. Colloidal gels with extracellular matrix particles and growth factors for bone regeneration in critical size rat calvarial defects. AAPS J. 2017. https://doi.org/10.1208/s12248-017-0045-0.
61. Chatzipetros E, Christopoulos P, Donta C, Tosios K, Tsiambas E, Tsiourvas D, et al. Application of nano-hydroxyapatite/chitosan scaffolds on rat calvarial critical-sized defects: A pilot study. Med Oral Patol Oral Cir Bucal. 2018. https://doi.org/10.4317/medoral.22455.
62. Chatzipetros E, Damaskos S, Tosios KI, Christopoulos P, Donta C, Kalogirou E-M, et al. The effect of nano-hydroxyapatite/chitosan scaffolds on rat calvarial defects for bone regeneration. Int J Implant Dent. 2021. https://doi.org/10.1186/s40729-021-00327-w.
63. de Molon RS, Fiori LC, Verzola MHA, Belluci MM, de Souza Faloni AP, Pereira RMR, et al. Long-term evaluation of alendronate treatment on the healing of calvaria bone defects in rats. Biochemical, histological and immunohistochemical analyses. Arch Oral Biol. 2020. https://doi.org/10.1016/j.archoralbio.2020.104779.
64. Al-Qutub M, Al-Omar N, Ramalingam S, Javed F, Al-Kindi M, Ar-rejaie A, et al. Guided bone regeneration using biphasic calcium phosphate with adjunct Recombinant human bone morphogenetic Protein-2 with and without collagen membrane in standardized calvarial defects in rats: A histologic and Biomechanical analysis. Int J Periodontics Restor Dent. 2016. https://doi.org/10.11607/prd.2376.
65. Gunes OC, Albayrak AZ, Tasdemir S, Sendemir A. Wet-electrospun PHBV nanofiber reinforced carboxymethyl chitosan-silk hydrogel composite scaffolds for articular cartilage repair. J Biomater Appl. 2020. https://doi.org/10.1177/0885328220930714.
66. Mano JF. Viscoelastic properties of Chitosan with different hydration degrees as studied by dynamic mechanical analysis. Macromol Biosci. 2008. https://doi.org/10.1002/mabi.200700139.
67. Torres PMC, Ribeiro N, Nunes CMM, Rodrigues AFM, Sousa A, Olhero SM. Toughening robocast chitosan/biphasic calcium phosphate composite scaffolds with silk fibroin: tuning printable inks and scaffold structure for bone regeneration. Biomaterials Adv. 2022. https://doi.org/10.1016/j.msec.2022.112690.

Publisher's Note

Springer Nature remains neutral with regard to jurisdictional claims in published maps and institutional affiliations.